Zito, A.; Wischmeier, M.; Carralero, D.; Manz, P.; Pérez, I. Paradela; Passoni, M.

Numerical modelling of an enhanced perpendicular transport regime in the scrape-off layer of ASDEX Upgrade

Published in:
Plasma Physics and Controlled Fusion

DOI:
10.1088/1361-6587/abfcb6

Published: 01/07/2021

Document Version
Publisher's PDF, also known as Version of record

Plasma Physics and Controlled Fusion

PAPER • **OPEN ACCESS**

Numerical modelling of an enhanced perpendicular transport regime in the scrape-off layer of ASDEX Upgrade

To cite this article: A Zito *et al* 2021 *Plasma Phys. Control. Fusion* **63** 075003

OPEN ACCESS
IOP Publishing
Plasma Physics and Controlled Fusion
Plasma Phys. Control. Fusion **63** (2021) 075003 (19pp)
https://doi.org/10.1088/1361-6587/abfcb6

Numerical modelling of an enhanced perpendicular transport regime in the scrape-off layer of ASDEX Upgrade

A Zito[1,2,*], M Wischmeier[1], D Carralero[3], P Manz[1,2], I Paradela Pérez[1,4], M Passoni[5] and the ASDEX Upgrade Team[6]

[1] Max-Planck-Institut für Plasmaphysik, Boltzmannstr. 2, 85748 Garching, Germany
[2] Physik-Department E28, Technische Universität München, Garching, Germany
[3] Laboratorio Nacional de Fusión, CIEMAT, Av. Complutense 40, 28040 Madrid, Spain
[4] Aalto University, Department of Applied Physics, Otakaari 1, 02150 Espoo, Finland
[5] Dipartimento di Energia, Politecnico di Milano, Via Ponzio 34/3, 20133 Milano, Italy
[6] See the author list 'H Meyer *et al* 2019 *Nucl. Fusion* 59 112014'.

E-mail: antonello.zito@ipp.mpg.de

Received 11 March 2021, revised 13 April 2021
Accepted for publication 29 April 2021
Published 25 May 2021

Abstract

A desirable scenario for future fusion devices is one in which dissipative processes in the scrape-off layer (SOL) are maximized, aiming to detach the divertor plasma. The access to such a regime in current devices is thought to be correlated to the increase of the perpendicular particle transport in the SOL. In this work we investigated numerically how increasing perpendicular transport globally affects the SOL plasma through the SOLPS-ITER code package. For this we modelled one L-mode discharge, performed at the ASDEX Upgrade tokamak, trying to obtain the most accurate fit to the experimental data at the outer midplane. Studying the plasma solutions and analyzing the resulting momentum and power balances in the SOL allowed to characterize how enhancing perpendicular SOL transport leads to the experimentally observed phenomena, i.e. the formation of a density shoulder at the midplane and the partial detachment of the divertor plasma. The results suggest that strong momentum losses caused by the increase of transport are able to explain the qualitatively observed detachment in the modelled discharge. The concurrent enhanced ionization of neutrals resulting from divertor recycling, triggered by an increase of radial energy transport in the SOL, can be invoked as a cause for the shoulder formation.

Keywords: scrape-off layer, perpendicular transport, particle and power exhaust, SOLPS-ITER, ASDEX Upgrade, density shoulder, divertor detachment

(Some figures may appear in colour only in the online journal)

* Author to whom any correspondence should be addressed.

1. Introduction

Understanding the physics of exhaust processes from magnetic confinement devices is one of the main open issues in nuclear fusion research [1]. Preventing exceedingly severe ion and heat fluxes from striking the plasma-facing components (PFCs) of future devices is mandatory in order to avoid melting and reduce erosion. This motivates targeted experiments in currently existing diverted tokamaks characterized by ITER-like plasmas and geometry. The goal is to find a way to reduce ion and heat loads striking the material surfaces to tolerable values under reactor-relevant conditions, namely large heating power and high density [2]. Recently, interest has risen about the possible effects of a regime of enhanced perpendicular transport in the scrape-off layer (SOL) in this regard [3].

In the literature enhanced perpendicular SOL transport has been widely attributed to advective transport mechanisms driven by turbulence and related to large density fluctuations in the SOL [4, 5]. It was proposed that such transport might manifest as dense localized filamentary structures which propagate radially in the SOL. Radial ballistic propagation of filaments in the SOL was indeed observed experimentally in a large variety of toroidal plasma devices and in different operating regimes, at velocities up to 500–1000 m s^{-1} [6].

An experimentally validated mathematical model explaining filamentary transport assumes that it is the effective electrical resistances in the SOL which determine the characteristic of filaments [7, 8]. The so-called divertor collisionalty parameter Λ_{div} was proposed as the main control parameter triggering a transition in the behaviour of filaments (i.e. in the existing relation between their size and radial propagation velocity) [9].

At the ASDEX Upgrade (AUG) tokamak, a regime of enhanced perpendicular SOL transport has been usually related to a flattening of the SOL density profile at the outer midplane, called a density shoulder. A correlation between the transition in radial propagation velocity of filaments, global intensity of perpendicular transport and formation of a density shoulder was, indeed, observed at AUG by Carralero *et al* [10–12]. An abrupt enhancement of perpendicular particle transport and the shoulder formation were seen to jointly take place when approaching sufficiently high density, at least in L-mode.

More recently the achievement of a partial detachment of the divertor plasma was also observed in the same conditions of enhanced perpendicular filament-driven transport [13]. This indicates a possible access to a highly dissipative regime for the SOL as well in such conditions.

In spite of being experimentally well-established phenomena, in the literature no agreement has been reached yet about the mechanisms leading to shoulder formation (see e.g. [12, 14]) and divertor detachment (see e.g. [15–17]). In particular, the correlation between such phenomena and perpendicular SOL transport still remains to be clarified. A detached divertor plasma is desired in future devices in order to reduce heat loads and erosion on the targets [3]. On the other hand, a density shoulder is usually related to a risk of severe main wall sputtering [12]. The search for an accurate predictive basis for the impact of perpendicular SOL transport on such phenomena is therefore essential, in view of the design of the PFCs in future devices.

Since the mechanisms relevant for the interlink between perpendicular transport, shoulder formation and divertor detachment are intrinsically complex, reliable numerical modelling is essential. In this work we performed a numerical experiment in order to investigate the way in which the increase of transport leads to the experimentally revealed features. For this we used the SOLPS-ITER code package [18–20], consisting in the coupling between the 2D multi-fluid plasma transport code B2.5 [21] and the latest parallelized version of the kinetic Monte Carlo neutral transport code EIRENE [22]. All simulations were performed as coupled B2.5-EIRENE runs.

We modelled two different scenarios from a single AUG L-mode discharge, already discussed in [13]. One is characterized by a weak perpendicular transport regime in the SOL and an attached divertor plasma. The other one is characterized by strong transport, a fully formed shoulder and a partially detached divertor plasma. We tried to obtain the most accurate fit to the experimental data at the outer SOL midplane for both scenarios. For this goal we developed a fitting algorithm which ensured a good match with the experimental radial SOL profiles taking into account the existing uncertainties in the measurements. The increase of perpendicular transport was modelled through a purely diffusive approximation, i.e. imposing an adequate effective particle diffusivity D_n.

The main experimental findings, i.e. the formation of a density shoulder at the outer SOL midplane and a partial detachment of the outer target, were successfully reproduced in the performed simulations following the increase of transport. We were able to explain both these phenomena as directly or indirectly following the transport enhancement. The analysis of the plasma solutions finally allowed us to make justified hypotheses on the possible physical mechanisms leading to the observed conditions.

In the section 2 the modelling work which was carried out to achieve realistic plasma solutions from the considered scenarios is described. In the section 3 the simulation results are presented. In the sections 4 and 5 the impact of perpendicular transport on shoulder formation and divertor conditions, respectively, is discussed according to the presented results. The summary of the work and a possible outlook are finally given in section 6.

2. Setup of the simulations

The preparation of the simulations consisted in setting up various input parameters with the goal of achieving physically reasonable results, i.e. in agreement with some measurements taken from the considered experimental scenarios. The main concern was to reproduce the radial plasma profiles at the outer SOL midplane. This would imply, indeed, modelling correctly the experimentally observed intensity of perpendicular transport as well.

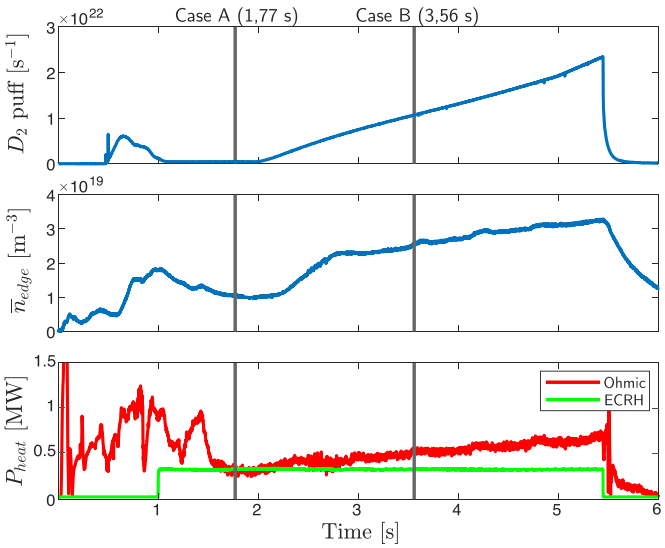

Figure 1. Some time traces for the AUG discharge #33341. From top to bottom: D_2-fueling level, line-averaged edge plasma density and heating power. The times at which the modelled scenarios were taken are highlighted by vertical lines.

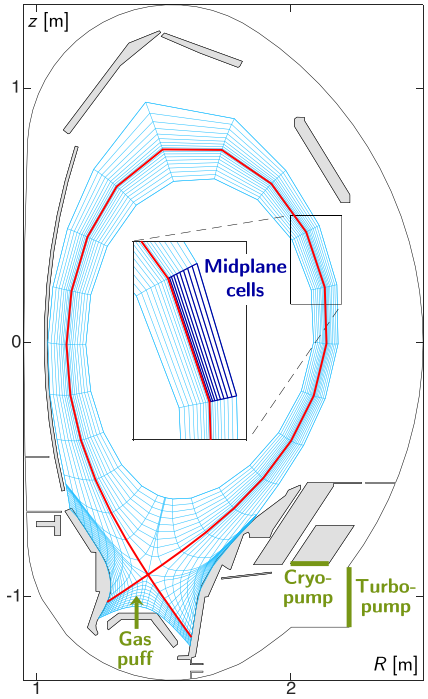

Figure 2. Magnetic-field-aligned computational grid used for the simulations. The outer midplane cells, to which many of the plots present in the text are referred, are highlighted in dark blue. Gas puff location and pumping surfaces are represented in green.

All drift terms in the B2.5 equations were disabled. The need of such simplification arose due to the exceedingly large time which would be needed for the convergence of the employed fitting procedure, with drifts activated.

2.1. Experimental scenarios

The considered experimental scenarios were taken from the AUG discharge #33341 (figure 1), which is the main experiment discussed in [13]. It is a pure deuterium L-mode density ramp, i.e. in which the fueling was gradually increased. In this way a wide range of values in divertor collisionality was covered. It featured a toroidal field of -2.52 T and a plasma current of 0.80 MA.

We tried to reproduce two different time intervals during the ramp, at 'low' and 'high' density respectively. The corresponding measurements were taken as input data for the simulations.

For low density/transport, from here on denoted as 'Case A', we considered the time $t = 1.77$ s. For high density/transport, from here on denoted as 'Case B', we considered the time $t = 3.56$ s. These are the same times at which the measurements discussed in [13] were taken. The second case featured a highly collisional divertor and a strong increase in intensity of radial filament propagation at the outer SOL midplane and, at the same time, the formation of a density shoulder and the achievement of a partially detached divertor plasma.

2.2. Computational grid

The employed computational grid, prepared for the considered scenarios, is shown in figure 2.

The grid has a resolution of of 48 poloidal cells and 18 radial cells. The grid cells are properly aligned with the equilibrium magnetic flux surfaces of the AUG discharge #33341 at the considered time slices. The reconstructed equilibrium was not exactly the same for the two times, but the small differences in the parameters relevant to exhaust physics such as the connection length, being less than 10%, justified the use of one single grid for both cases. As 'outer midplane' we set the row of cells at a poloidal location slightly higher than the equatorial midplane (blue cells in figure 2). Here most of the plasma edge diagnostics, including the ones considered in this work, actually measure the radial plasma profiles [13].

The source for the deuterium molecules is located in the divertor region, in front of the dome baffle (green arrow in figure 2). This location resembles the position of the valves employed in the experiment for the gas puff. The source of neutrals at the puffing location is mono-energetic, with injected neutrals having a fixed energy equal to the thermal energy at room temperature. Active pumping takes place at the actual pumping surfaces in the divertor region, i.e. at the turbo- and cryopump (green lines in figure 2). We employed a pumping model for the neutrals which was experimentally validated at AUG. Neutral absorption on the turbo- and cryopump surfaces was modelled by albedo coefficients of 0.993 and 0.7 respectively. These values roughly reproduce the experimentally observed pumping speeds for deuterium neutrals at both pumping surfaces. The finite conductances for neutral transport existing between the various chambers in the divertor region were emulated by imposing fictitious ducts.

The standard set of atomic and molecular processes in EIRENE for pure deuterium SOLPS runs was used (see table 1). This set includes electron-impact ionization (EI), recombination processes (RC), molecular dissociation

Table 1. Atomic and molecular volumetric processes modelled by EIRENE in the performed simulations. All these are modelled using the rate coefficients present in the databases AMJUEL and HYDHEL.

Reaction	Type
$D + e \rightarrow D^+ + 2e$	EI
$D_2 + e \rightarrow D_2^+ + 2e$	EI
$D_2 + e \rightarrow D + D^+ + 2e$	DS-EI
$D_2^+ + e \rightarrow D^+ + D^+ + 2e$	DS-EI
$D^+ + e \rightarrow D$	RC
$D_2^+ + e \rightarrow D + D$	DS-RC
$D_2 + e \rightarrow D + D + e$	DS
$D_2^+ + e \rightarrow D^+ + D + e$	DS
$D + D^+ \rightarrow D^+ + D$	CX
$D_2 + D^+ \rightarrow D_2^+ + D$	CX
$D_2 + D^+ \rightarrow D_2 + D^+$	EL

processes (DS), charge-exchange collisions (CX) and elastic scattering (EL).

Some relevant boundary conditions which were used are constant values of electron/ion heat fluxes crossing the core plasma boundary (see next subsection) and sheath conditions at the plasma/target interfaces in the divertor (i.e. parallel flow velocity larger than or equal to the local sound speed). Additionally, the default choice for the parallel heat flux limiters was used [18].

2.3. Optimization of the input parameters

The main physical inputs to be chosen as input parameters for SOLPS simulations are input power, density level and an assumption for the perpendicular transport coefficients.

Setting the input power in the computational domain was straightforward. We imposed given values of electron/ion heat fluxes on the core plasma boundary in order to model the power leaving the core plasma region. The sum of these corresponds to the total power entering the edge plasma region. We assumed that such power is carried half by electrons and half by ions. The total heating power for the cases A and B is, respectively, 620 and 820 kW (see figure 1). We considered the same estimate for the fraction of radiated power in the core stated in [13], i.e. 0.15 for the case A and 0.25 for the case B. So, the total input power in the computational domain for the two cases was assumed as 520 and 610 kW respectively.

More challenging were the specification of the density and a choice for the perpendicular transport coefficients. A number of uncertainties had to be faced in this regard.

First, we chose to impose the density through a feedback scheme in the simulations. Namely, arbitrarily chosen values for the separatrix electron density $n_{e,sep}$ at the outer midplane had to be defined: these could be achieved through a feedback mechanism regulating the gas puff source during the run. However, the existing methods of magnetic reconstruction at AUG allow the knowledge of the position of the separatrix only to within an error of several mm. This implies a strong uncertainty in the estimation of the separatrix density $n_{e,sep}$ at the outer midplane in the considered experimental scenarios. To handle this issue, we considered the position of the separatrix R_{sep} as unknown *a priori*, and took the experimental radial plasma profiles at the outer midplane as function of the major radius R as only experimental basis. We chose the signals provided by the integrated data analysis (IDA) for the electron density profiles, which are derived from the combination of different heterogeneous diagnostics [23, 24].

Second, SOLPS-ITER assumes an anomalous perpendicular transport. So, empirically-derived radial profiles for the perpendicular transport coefficients need to be defined by the user (namely, for all radial locations of the computational domain). The most crucial issue was achieving a correct fit for the experimental radial density profiles for all modelled cases. Therefore, since first-principle-based theories for predicting the transport coefficients required for modelling filamentary transport are missing, a fine tuning of the employed perpendicular particle transport was needed.

In detail, SOLPS-ITER can make use of a particle diffusivity D_n and an anomalous pinch velocity v_n [20]. The first one defines a diffusive transport component which is proportional to the radial density gradient. The second one, instead, defines a real advective transport component proportional to the density itself. We chose to model the increase of transport solely through the imposition of an adequate radial profile of the particle diffusivity D_n as the use of an anomalous pinch velocity would be numerically problematic. In the simulations such a coefficient intends then to average the effects of the intermittent filament-driven advective transport on a sufficiently long time scale, assuming the meaning of an 'effective' particle diffusivity. In other words, it was used to simulate any processes related to radial particle transport, regardless of their actual nature (which might be diffusive of advective).

A diffusive component of the perpendicular energy transport was also assumed, by means of thermal diffusivities χ_e, χ_i. The assumed χ_e, χ_i profiles were based upon the setup of similar SOLPS simulations of L-mode discharges at AUG [25], without carrying out a further fine tuning. Indeed, it is generally accepted that the radial propagation of filaments does not affect the temperature-gradient-driven thermal transport [13].

In order to deal with these issues we developed a fitting procedure for such input parameters, which is described in detail in the appendix A. We satisfactorily resolved the uncertainty on the position of the separatrix and the arbitrariness of the choice of the perpendicular particle transport coefficients. The employed strategy was coupling the experimental knowledge of the radial plasma profiles at the outer midplane with the results of the simulations in a self-consistent way. This allowed us to choose the most appropriate estimate for the position of the separatrix (and hence for $n_{e,sep}$) and reproduce the experimental radial density profiles at the outer midplane. The latter was done through an algorithmic optimization of the radial profiles of D_n.

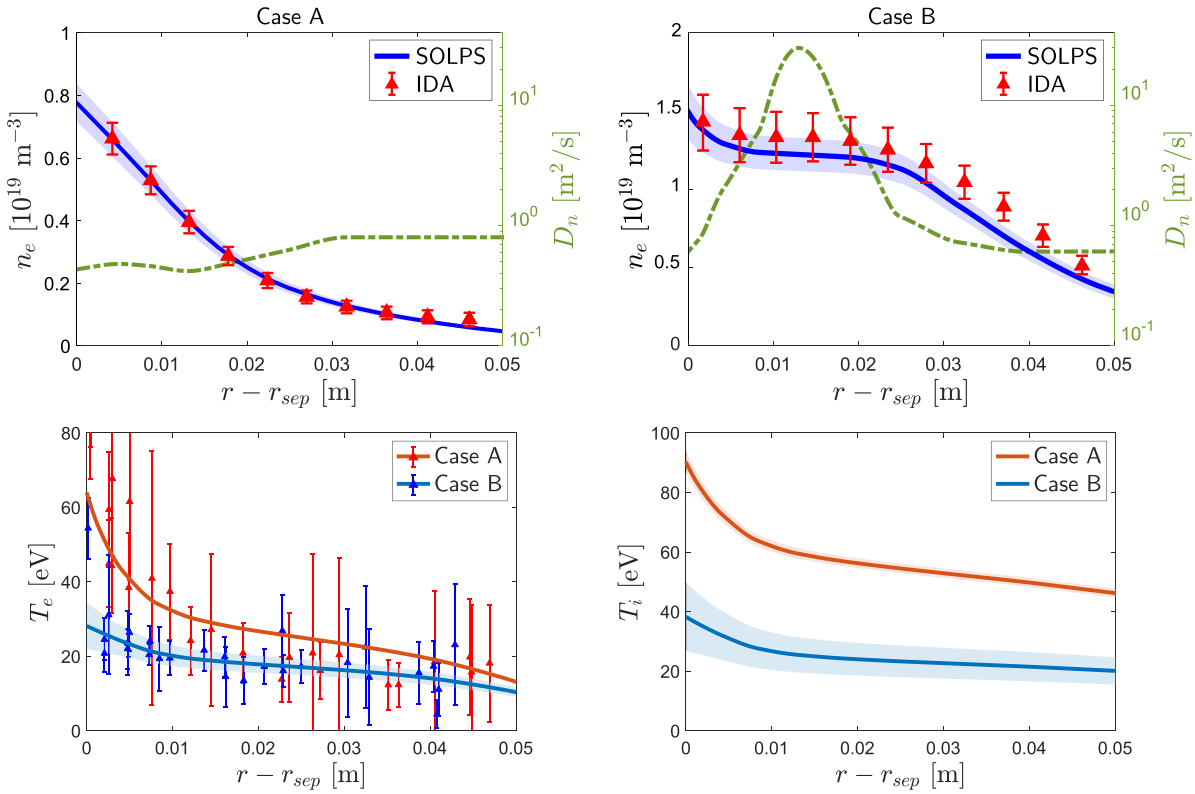

Figure 3. Top plots: modelled radial density profiles at the outer midplane (blue solid lines) and comparison with the experimental IDA data (red triangles). Left plot for case A and right plot for case B. The imposed particle diffusivity for both cases is represented by the green dashed lines. Bottom plots: modelled radial electron and ion temperature profiles at the outer midplane (solid lines) for both cases in different colours. Experimental T_e data by Thomson scattering (TS) for both cases are depicted as triangles. The shadowed areas describe the confidence bands of the presented profiles, achieved accounting for the experimental uncertainty of $n_{e,sep}$.

2.4. Results of the employed fitting algorithm

The results of the algorithm included the most reliable density levels to be imposed in the final simulations, and the relative uncertainties (i.e. the values of $n_{e,sep}$ and the relative lower and upper bounds). This allowed us to present the results for all modelled cases in confidence bands resulting from the simulations being run for the 'central' $n_{e,sep}$ values as well as for the relative lower/upper bounds. These are depicted as shadowed areas in the plots presented later in the text.

Figure 3 shows the good agreement achieved between modelled and experimental radial density and temperature profiles at the outer SOL midplane for both cases. For the density profiles, this was precisely the goal of the employed fitting algorithm: the deviation of the modelled values from the experimental values is not larger than 10% at all radial locations. The diffusivity profiles required for this, resulting from the employed fitting algorithm, are also reported in the top plots. We can note that:

- For case A (low density, no density shoulder) the best assumption for the position of the separatrix corresponded to a separatrix density of $0.78(\pm 0.06) \times 10^{19}$ m^{-3}. The nearly exponentially decaying radial density profile in the SOL could be reproduced by means of a quite flat profile for the particle diffusivity, with values of about 0.5–1 m^2 s^{-1}, i.e. of the order of the Bohm scaling.
- For case B (high density, fully formed density shoulder) the best assumption for the position of the separatrix corresponded to a separatrix density of $1.52(\pm 0.18) \times 10^{19}$ m^{-3}. The region with flattened density could be reproduced by means of a strong localized increase of the particle diffusivity, up to several tens of m^2 s^{-1}.

The unusually high values of the perpendicular transport coefficient used for the case B are supported by a recently published transport model by Manz *et al* [26]. This model interprets the advective radial propagation of microscopic structures with some typical radial velocity (such as filaments) through a diffusive approximation, including the effects of time intermittency by means of some auto-correlation time. It suggests that a perpendicular transport dominated by the fast radial ballistic propagation of filaments could be described through a time-averaged steady-state effective particle diffusivity of the order of tens of m^2 s^{-1}. Such order-of-magnitude estimate is, indeed, in reasonable agreement with what achieved with the present SOLPS results.

3. Overview of the numerical plasma solutions

We explored the converged numerical plasma solutions for the modelled cases to study in detail the physical origin of the density shoulder and the interlink between increase of

transport and divertor detachment, at least in the performed simulations.

Regarding the second issue, it is worth to mention that in L-mode discharges, like the one from which the considered scenarios are taken, the mere increase of the plasma density might be alone sufficient to promote a detached regime. We tried then to disentangle the effects of a mere increase of density from the effects which purely follow the enhancement of transport. Besides the real scenarios (cases A, B in the last section), a fictitious 'intermediate' scenario was modelled as well: this corresponds to a 'high' density regime (i.e. imposition of the same $n_{e,sep}$ value as in the case B) but characterized by 'low' transport (i.e. imposition of the same radial D_n profile as in the case A). Later in this section, the results regarding the divertor conditions will include this intermediate situation as well.

3.1. Radial energy transport at the outer SOL midplane

The first matter of investigation was the possible impact of the increase of radial particle transport on the radial energy transport at the outer SOL midplane. An increase of radial energy transport was indeed observed experimentally in the considered high density/transport scenario [13]. This was attributed to the fact that, in their radially-directed motion, filaments might directly carry some energy with them towards the far SOL.

SOLPS-ITER is suitable for investigating the possible impact of filament-driven transport on the energy fluxes. The modelled radial energy flux density is [20]

$$q_\perp = -n_e\left(\chi_e\frac{\partial T_e}{\partial r}+\chi_i\frac{\partial T_i}{\partial r}\right)+\frac{5}{2}\Gamma_\perp(T_e+T_i). \qquad (1)$$

The first component, i.e. the conductive component, which is not expected to be directly affected by the filament propagation, is not related to the particle transport intensity, but only described by the thermal diffusivities χ_e, χ_i. The second one, i.e. the convective component, which is the one expected to increase, is indeed sensitive to an increase of the radial particle flux. Therefore, an increase of the last component following an increase of the particle diffusivity is plausible.

We investigated the possible impact of the increase of radial particle transport on radial energy transport at the LFS (low field side) of the SOL by performing an energy balance on a domain radially extended in the SOL and poloidally extended about the outer midplane (yellow volume in figure 4).

At any radial location $r-r_{sep}$, the decrease of the amount of energy $Q_\perp$ which is still present at the midplane is balanced by the cumulative parallel losses $Q_\parallel$ and the cumulative volumetric energy losses, i.e. occurring between $r-r_{sep}=0$ and that given radial location.

The energy still present at the midplane at each radial location is computed as

$$Q_\perp(r-r_{sep}) = \sum_{poloidal} q_\perp A_\perp \qquad (2)$$

i.e. as the product between modelled radial energy flux density $q_\perp$ entering each cell from its left boundary and surface area

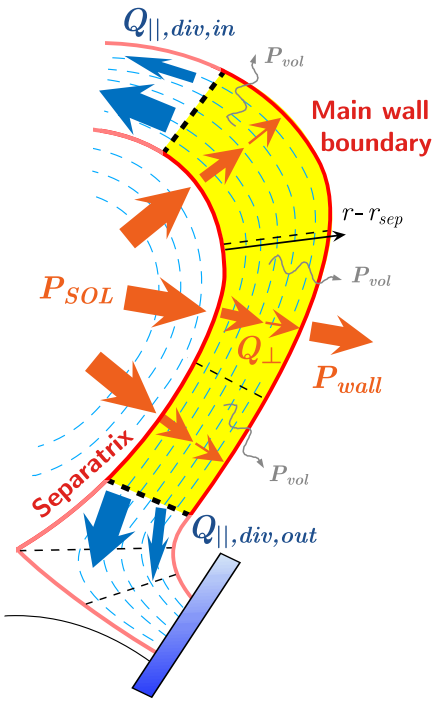

Figure 4. Geometry in which the calculations concerning the energy balances at the LFS SOL were performed.

$A_\perp$ of such boundary. The sum is performed over all the cells present in the poloidal extension of the considered domain.

The calculation yielding the cumulative parallel losses is

$$Q_\parallel(r-r_{sep}) = \left[2\pi\int_0^{r-r_{sep}}\left(\frac{B_\theta}{B}q_\parallel\right)R(r')\,dr'\right]_{\text{div,in}} + \left[2\pi\int_0^{r-r_{sep}}\left(\frac{B_\theta}{B}q_\parallel\right)R(r')\,dr'\right]_{\text{div,out}}. \qquad (3)$$

The poloidal projection of the modelled parallel energy flux density $q_\parallel$ is integrated in the toroidal and radial directions. The net parallel energy loss is obtained summing the energy flows calculated in this way crossing top and bottom boundaries of the considered domain, i.e. leaving the domain and directed to inner and outer divertor respectively.

The competition between radial energy transport and parallel energy losses resulting from such balance is visible in figure 5 for both cases. All values are normalized to the input power P_{SOL} in the balance domain, i.e. the energy ejected from the core plasma through the separatrix and crossing the left boundary of the domain. P_{SOL} corresponds to 508 and 538 kW for cases A, B respectively, out of a total input power in the computational domain of 520 and 610 kW respectively.

At the separatrix, $Q_\perp/P_{\text{SOL}}$ is equal to one by definition. Then, going further the fraction of energy which is still present at the midplane SOL decreases as the cumulative parallel losses towards the divertors and the volumetric losses increase. At high density/transport a large fraction of energy ejected from the core evidently remains at the midplane SOL also several cm far from the separatrix. As expected, this is because

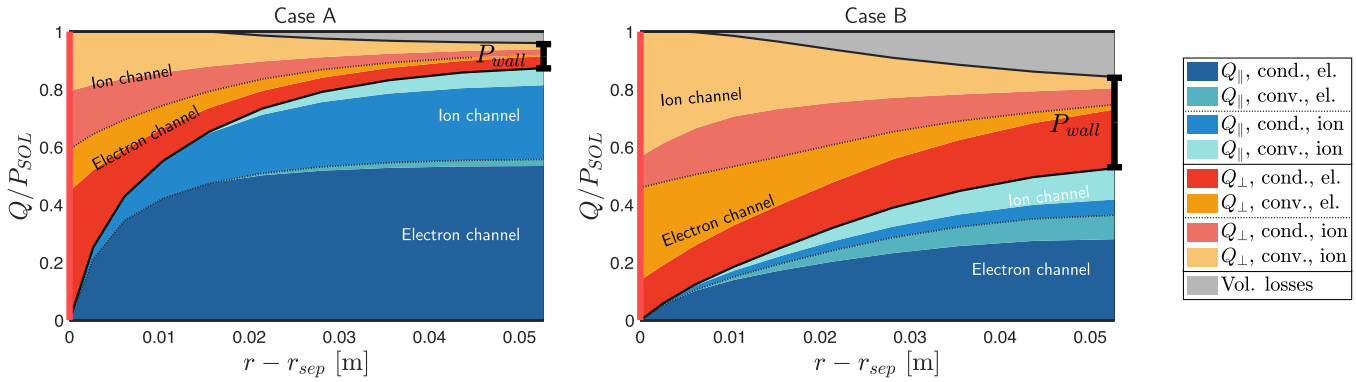

Figure 5. Results of the energy balance at the LFS SOL. Solid borders in the plots help distinguish between (1) components of the cumulative parallel energy loss between the separatrix and the location $r - r_{sep}$ (in blueish colours), (2) components of the energy still present in the balance volume at the location $r - r_{sep}$ (in reddish colours) and (3) cumulative volumetric energy loss between the separatrix and the location $r - r_{sep}$ (in grey). Dotted borders help distinguish between electron and ion channels. Radial coordinates are remapped to the one at the outer midplane.

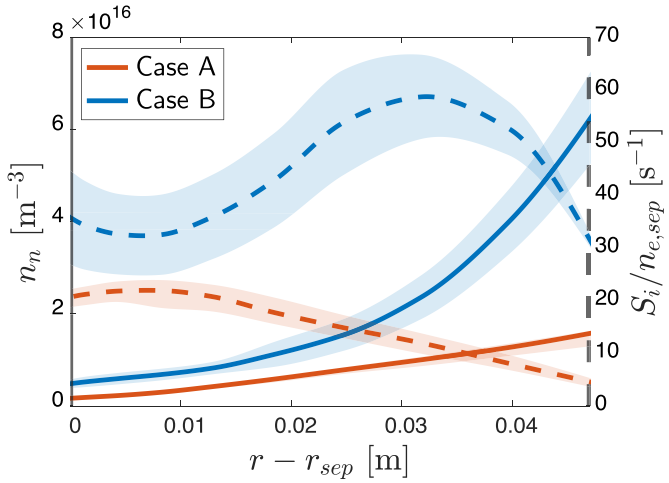

Figure 6. Neutral population (solid lines) and source of plasma particles by ionization (dashed lines) at the outer SOL midplane cells of the computational domain, the latter normalized to $n_{e,sep}$.

of a strong increase of the fraction of energy radially convected in the first cm of the SOL, i.e. precisely where the radial particle transport was increased. Because of this, the fraction of energy $Q_{\mathrm{wall}}/P_{\mathrm{SOL}}$ which reaches the outer boundary of the domain increases from less than 10% at low density/transport to about 30% at high density/transport. This result agrees very well with the experimental power balance of the same scenarios presented in [13] and more in detail in [27].

3.2. Ionization at the outer SOL midplane

One aspect possibly related to the shoulder formation is the local ionization at the SOL midplane. We focused then on evaluating a possible increase of the local particle source at the midplane, between cases A, B, by ionization of the neutrals.

The total neutral density n_n and the total particle source by ionization S_i at the midplane cells of the computational domain were extracted for both cases (figure 6). The ionization source is plotted as dashed lines, normalized to the density at the separatrix to account for the increase of the ionizations merely related to the increase of density.

At low density/transport S_i increases continuously towards the separatrix, following a decrease of the ionization mean free path (caused in turn by the increase of plasma density and temperature). At high density/transport, instead, an evident 'ionization peak' appears. Interestingly, the radial location of such peak corresponds exactly to where the flattening starts degrading (top right plot in figure 3). This is consistent with the neutral population (solid lines) decaying much faster, when approaching the separatrix, at high density/transport rather than at low density/transport.

3.3. Ion and heat loads onto the outer target

The second figure of merit for the numerical investigation was the impact of the enhanced transport on the divertor conditions. Such impact was experimentally revealed [13]: while raising the density in the AUG discharge #33341, the one under investigation, the divertor plasma was seen to transit from a high-recycling regime to a partially detached regime, at least for the outer target. This was manifested after observing the rollover of the ion flux onto the target.

We analyzed then the outer divertor target conditions in order to see if this was reproduced by the performed simulations. Figure 7 shows the total particle (i.e. ion) flux density and heat flux density striking the outer target surface for all cases, including the 'intermediate' case characterized by a high density without the transport enhancement. A quantitative reproduction of the divertor conditions was out of the scope of this work, especially since the simulations were performed without considering the impact of drifts. Nevertheless, the modelled ion flux density profiles are in good qualitative agreement with the Langmuir probe data from the modelled discharges [13]. The modelled heat flux density profiles, instead, slightly underestimated the experimental ones [13].

At high density, high transport, both ion and heat flux profiles onto the target are visibly flattened. Their peak value is decreased and radially shifted outwards. This is sufficient to

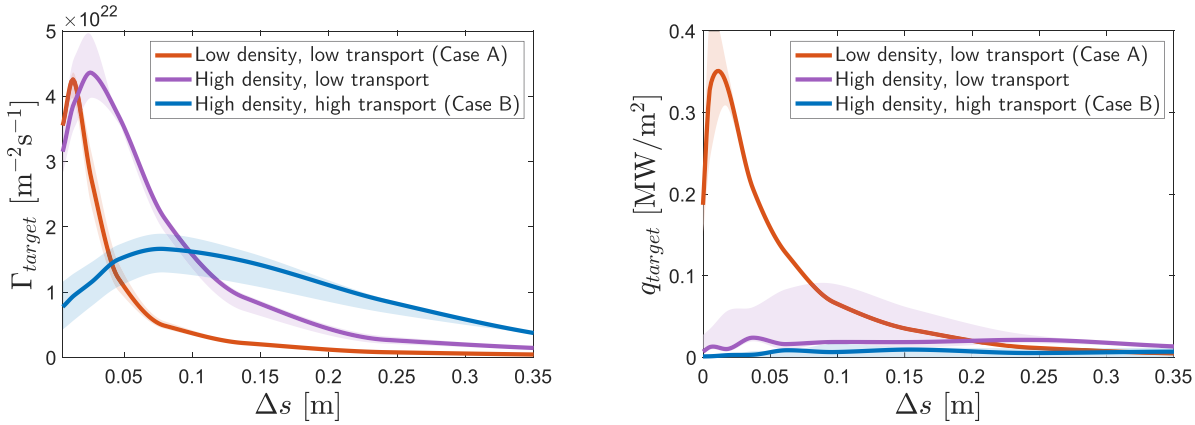

Figure 7. Modelled particle (i.e. ion) flux density (left) and heat flux density (right) striking the outer target in normal direction for all cases. Δs represents the radial distance, onto the target surface, from the separatrix strikepoint.

say that a pronounced detachment state has been achieved by the simulations in this scenario [28]. In the high density scenario without enhanced transport, instead, the heat flux profile is already strongly flattened, while the ion flux profile is still peaked close to the separatrix strikepoint. This is a strong indication that the enhancement of perpendicular transport has played a crucial role in dropping the ion flux onto the target, over the mere density increase: only after the increase of transport, $n_{e,sep}$ being the same, the peak ion flux is decreased roughly by half.

3.4. Power losses in the SOL

As final task of our exploration of the numerical plasma solutions, we tried to quantify the dissipation of momentum and power along the SOL and characterize the relative loss mechanisms. The goal was understanding whether the main role in achieving the experimentally revealed highly dissipative regime in the high transport scenario [13] was played by the mere increase of density or specifically by the increase of perpendicular transport.

First, we quantified the power losses occurring in the SOL plasma before reaching the targets. This was done by extracting, from the plasma solutions, the energy flows crossing the main boundary surfaces of the computational domain. We took the total power P_{SOL} crossing the separatrix as reference for the input power into the SOL. Part of this power, P_{wall}, is radially transported towards the main chamber wall. Another part, P_{targets}, is parallel transported towards the divertor targets. The remaining part, $P_{\mathrm{vol}} = P_{\mathrm{SOL}} - P_{\mathrm{wall}} - P_{\mathrm{targets}}$ is the total volumetric power loss.

In [29] a power loss factor was defined as the total fraction of the SOL input power being dissipated before reaching the targets, i.e. as

$$f_{\mathrm{power}} \equiv 1 - \frac{P_{\mathrm{targets}}}{P_{\mathrm{SOL}}}. \tag{4}$$

We calculated this factor for all cases, obtaining $f_{\mathrm{power}} = 0.36$ for the low density, low transport case, $f_{\mathrm{power}} = 0.83$ for the high density, low transport case, and $f_{\mathrm{power}} = 0.91$ for the high density, high transport case. Power losses are, as expected, quite relevant at high density, reaching a dissipation of over the 80% of the total input power into the SOL. This is mainly by means of an increase of radiation losses by plasma-neutral interactions. However, the value which was calculated for the 'real' high density, high transport case is not much larger than the one which would be achieved in the same scenario but without transport enhancement (0.91 vs. 0.83). Therefore, power losses are achieved mainly with the mere increase of density rather than with the enhancement of transport.

3.5. Parallel momentum losses in the SOL

Finally, we investigated the intensity of momentum losses occurring in the plasma flow from an upstream location (outer midplane) to a downstream location (outer target) and their correlation with the increase of transport. To do this, we looked directly at the fluid equations solved by SOLPS-ITER.

We employed a two-point-model (2PM)-like approach, relating the plasma profiles between the upstream and downstream locations. Integral two-point relations were derived considering the same treatment developed by Kotov and Reiter in [30]. Namely, we integrated the parallel momentum balance equation solved by B2.5 between such two poloidal locations, assuming a steady-state situation (i.e. assuming the numerical convergence being reached). The difference in total pressure

$$p_{\mathrm{tot}} = n_e(T_e + T_i) + m_i n_e v_{\parallel}^2 \tag{5}$$

i.e. the sum of static and dynamic pressure, between downstream and upstream, for each flux tube, results in a total momentum source term (i.e. integrated between upstream and downstream). A brief derivation of such momentum balance analysis is given in the appendix B. The results for all cases are shown in figure 8.

While at low density momentum losses are negligible, moving on to high density a strong increase of the total loss was found, mainly concentrated in the near SOL. After the transport enhancement, profile and relative intensity of momentum losses are similar. However, the peak of the pressure profile on the target is quite radially shifted to the far SOL. As a result,

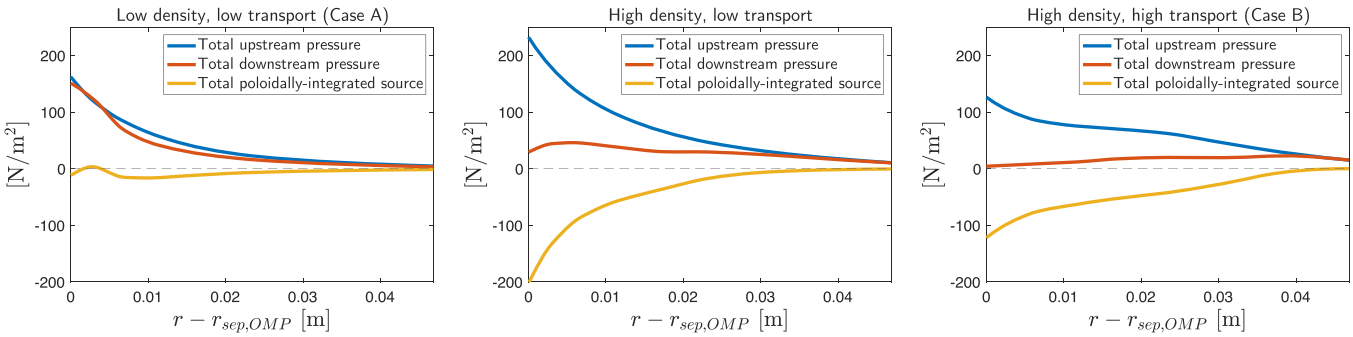

Figure 8. Results of the momentum balance between upstream and downstream for all cases. For each flux tube the difference between downstream and upstream pressure is equal to the total poloidally-integrated momentum source. Radial coordinates are remapped to the one at the outer midplane.

pressure is completely removed from the flux tubes close to the separatrix when approaching the target, differently from the high density, low transport case, where some amount of pressure was still present on the near-strikepoint portion of the target. In section 5 the physical mechanisms leading to such momentum losses will be investigated in more detail.

4. Perpendicular transport and density shoulder formation

The presence of a density shoulder at the outer SOL midplane in conditions of enhanced perpendicular transport, widely observed experimentally, was correctly reproduced by the performed simulations (figure 3). The performed SOLPS modelling could not provide details about turbulence and specific characteristics of filaments, although their presence might be quite well simulated through an increase of the particle diffusivity in the SOL [26]. Nevertheless, analyzing the plasma solutions allowed us to discuss the possible physical mechanisms relating shoulder formation and increase of transport.

4.1. Experimental evidences

No agreement has been reached in the literature yet about the mechanisms relating perpendicular transport and shoulder formation. It is accepted that changes in the divertor collisionality Λ_{div} lead to changes in filament characteristics and, hence, to a transition in the global perpendicular SOL transport intensity [11]. However, it is still debated if this is sufficient for forming the shoulder.

In the already mentioned studies performed with pure deuterium L-mode plasmas at AUG by Carralero *et al* [12], an increase of Λ_{div} over some threshold value appears as a necessary condition for the shoulder formation. The transition in perpendicular transport occurring at high collisionality was seen to directly contribute, in first instance, to bring more particles towards the far SOL. Following Lipschultz *et al* [31], it was assumed that the consequent rise of density in the far SOL would make it more 'opaque' to the neutrals. This would contribute to ionize much more neutrals close to the wall rather than close to the separatrix. Consequently, the local volumetric particle source would be enhanced, increasing even further the far SOL density and making the plasma here even more opaque. This 'ionization feedback loop' would sustain the elevated plasma density in the far SOL.

Similar studies performed with L-mode plasmas at JET by Wynn *et al* [14] point out that some additional mechanism would be needed. The increase of Λ_{div} (and hence of perpendicular filament-driven transport) was found to be not sufficient for sustaining the shoulder formation. Increasing Λ_{div} through a ramped fueling, the flattening of the profiles was seen to scale with the collisionality, in agreement with the AUG results. Increasing, instead, Λ_{div} by cooling down the divertor through an increased nitrogen seeding, no shoulder was observed. The only quantity which was seen to correlate well with the presence of a shoulder in a wide range of scenarios is the outer divertor Balmer D_α line emission magnitude. This is a proxy for the amount of ionization processes in the divertor, i.e. for the intensity of neutral recycling at the targets. This led to assume that any mechanisms involved in the shoulder formation would need to be related with divertor recycling.

4.2. Role of far SOL ionization

The results about far SOL midplane ionization (figure 6) confirm the presence of an ionization peak in the far SOL, as assumed by Carralero *et al*. This would effectively prevent neutrals from reaching the separatrix. The localized increase of ionization processes would provide the required additional plasma particles. This finding supports the assumption of an ionization feedback loop playing a role in forming the shoulder.

Wynn *et al* pointed out that ionization in the far SOL might be enhanced as a consequence of an increased density in the far SOL, rather than being its cause. If this was true, another physical mechanism would be needed for the 'existence' of more particles in the far SOL. Let's consider a radial balance equation for particles in the simple form [29]

$$\frac{\partial n_e}{\partial t} = D_n \frac{\partial^2 n_e}{\partial r^2} - \frac{n_e}{\tau_{\parallel}} + S_i \qquad (6)$$

with parallel loss term $\frac{n_e}{\tau_{\parallel}}$, being $\tau_{\parallel}$ a characteristic parallel loss time. If the local particle source by ionization S_i really does not play a causal role, then such a balance could be altered only

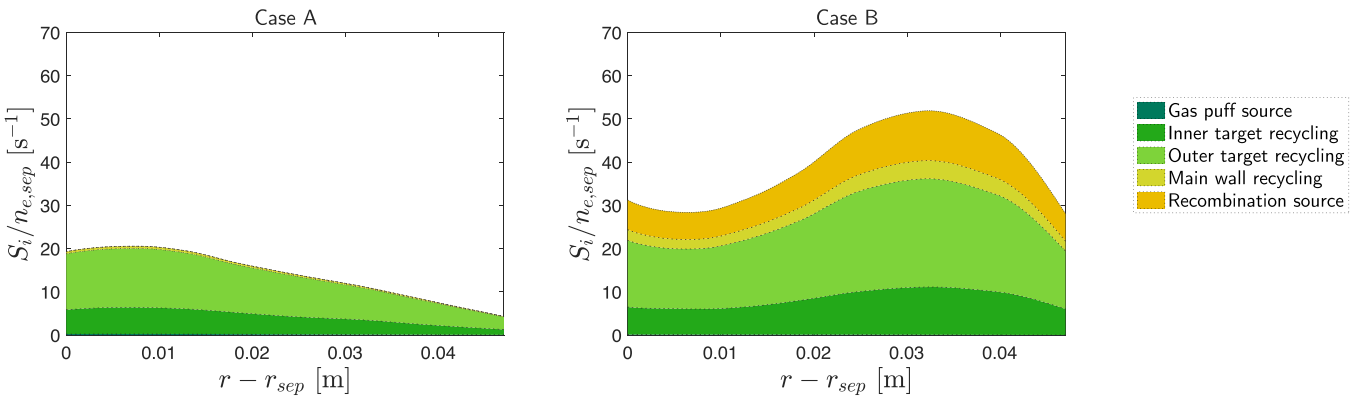

Figure 9. Components of the ionization particle source, at the outer SOL midplane cells of the computational domain, in terms of the origin of the ionized neutrals (i.e. neutrals coming from the gas puff source, recycled from the material surfaces or resulting from the recombination processes), represented in different colours.

through a direct increase of the radial particle flux (first term on the R.H.S. of the equation (6)) over the parallel losses (second term on the R.H.S. of the equation (6)). We found out that, while the radial particle flux at the outer midplane increased when increasing the particle diffusivity, the ratio of radial-to-parallel particle flux is not substantially changed. This means that the increase of radial particle transport at the midplane is compensated by a concurrent increase of the parallel losses towards the divertor. What 'feeds' the shoulder, at least in the performed simulations, cannot be anything other than an increase of S_i.

This assumption is further supported by the strong decrease of the ion temperature in the far SOL when the shoulder is present (bottom right plot in figure 3). This is consistent with the picture of hot ions ejected from the separatrix joining a population of cold ions being originated in the far SOL by ionization of neutrals, already discussed in [12].

4.3. Role of radial energy transport

Additional aspects of the numerical plasma solutions support the assumption of the ionization loop in the far SOL in conditions of enhanced perpendicular transport. The increased radial energy transport (figure 5) might be invoked as a further, if not the main, feature triggering the formation of the ionization peak. Namely, only after the transport enhancement a larger amount of energy can be transported towards the far SOL (where a larger population of neutrals is present). Therefore, there is more possibility of supplying the energy cost needed for each ionization event, implying an increase of the number of ionizations per electron in the far SOL.

This assumption is further supported after decomposing the volumetric energy losses (from the electron channel) in the high-transport solution: in the far SOL they are predominantly due to electron-impact ionizations.

Additionally, this might even explain why Wynn *et al* encountered highly collisional scenarios without a density shoulder in nitrogen-seeded plasmas. Namely, reaching high values of Λ_{div} might have been sufficient to provide a strong filament-driven radial particle transport. However, this could not translate into a larger amount of energy transported towards the far SOL because of increased impurity radiation due to nitrogen. As there was not enough energy available in the far SOL to account for the cost due to more ionization, the activation of the ionization feedback loop might have been not possible.

4.4. Role of main wall and divertor recycling

After suggesting the first necessary 'ingredient' for the ionization loop, i.e. the energy, we investigated the possible origin of the second one, i.e. the neutrals.

It is usually assumed that, in conditions of enhanced perpendicular transport, an important source of neutrals in the far SOL is due to the onset of a recycling condition at the main chamber wall. Namely, the larger fraction of ions striking the wall would result in a larger amount of recycled neutrals emitted towards the plasma. Such situation, first observed in Alcator C-Mod by LaBombard *et al* [32], is referred to as main wall recycling.

SOLPS allows to characterize the volumetric sources driven by atomic/molecular processes, computed by EIRENE, in terms of the physical origin of the involved neutrals. So we were able to decompose the ionization source profiles of plasma particles at the outer midplane cells of the domain (dashed lines in figure 6) in terms of the origin of the neutrals which were ionized (figure 9).

In both cases the ionization source originates only to a small part from neutrals recycled at the wall. The gas puff source is also negligible in contributing to the total ionization source (about 1%). Most of the ionized neutrals come from divertor recycling. An increase of main wall recycling, in absolute quantity, is actually present at high density/transport, following the increase of the ion flux striking the wall, in agreement with many experimental observations. However, it is still not dominant in providing the neutrals which are ionized at the midplane (less than 10% of the total). Therefore, the existence of a localized increase of the ionization source in the case where the shoulder is present seems to not be strongly affected by the presence of main wall recycling.

This result, however, is in contrast with already published EMC3-EIRENE modelling works, such as the one performed by Lunt *et al* [33]. There it was argued that the presence (i.e. the activation) of the main wall recycling mechanism is a necessary condition for forming a density shoulder. A possible underestimate of this contribution in SOLPS-ITER could be explained by the fact that, in the modelled case, the computational grid cannot be actually extended up to the physical walls, while in EMC3-EIRENE this is possible. Thus, we think that this aspect would need a more careful evaluation.

The major relevance of the (outer) target recycling source, for the neutrals ionized at the midplane, is consistent with the assumption of Wynn *et al* of any major mechanism responsible for shoulder formation to be related with divertor recycling. In order to investigate this in more detail we compared, for the case where the shoulder is present, the ionization front of the neutrals recycled at the outer target and the poloidal dependence of the total pressure drop (the last one evaluated in the section 3.5). Figure 10 shows the contour levels describing the fraction of neutrals recycled at the outer target which have ionized after being emitted towards the SOL plasma. The poloidal dependence of the total pressure drop is shown plotting a 'local' momentum loss factor, defined in a similar way as in [29], as

$$f_{\mathrm{mom,local}}(x) \equiv 1 - \frac{p_{\mathrm{tot}}(x)}{p_{\mathrm{tot,up}}}. \tag{7}$$

This quantifies the decrease of total pressure (equation (5)) while travelling from upstream (i.e. outer midplane) towards the target along a poloidal coordinate x for each flux tube, with respect to the total pressure upstream $p_{\mathrm{tot,up}}$ at that flux tube.

The strong momentum losses which occur in this case along the SOL, described in the section 3.5, are concentrated close to the targets, where plasma-neutral interactions are most relevant (see next section). Therefore, at the poloidal location at which most of the neutrals recycled from the target have been ionized, the pressure is more or less the same as at the midplane.

The fact that pressure is roughly conserved between midplane and ionization front of the target-recycled neutrals suggests a correlation between density shoulder and divertor neutral recycling, as first assumed by Wynn *et al* [14]: it is the recycling profile at the outer target which might determine the midplane profile.

Pressure conservation between midplane and divertor ionization front implies, indeed, the conservation of the shape of the radial density profile [29]. At the location of the ionization front of the target-recycled neutrals, this is already flattened. This suggests that the shape of the midplane profile is merely controlled by the plasma conditions at the ionization front. And what takes place at the ionization front of the target-recycled neutrals must be, in turn, correlated to the target recycling profile (through divertor geometry and neutrals opacity).

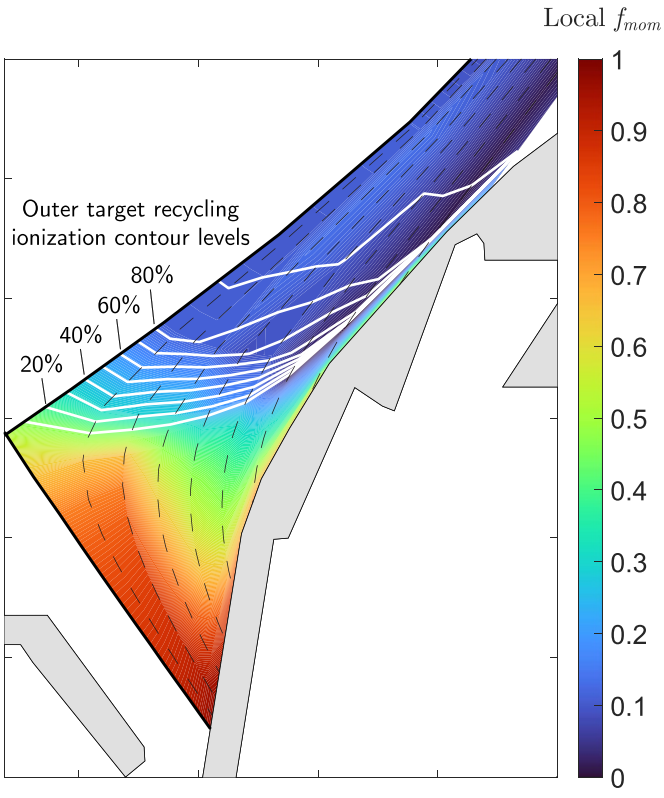

Figure 10. 2D distribution of the local momentum loss factor in the high density, high transport scenario (case (B). $f_{\mathrm{mom,local}} = 1$ means pressure completely removed from a flux tube. White contours represent the fraction of neutrals recycled at the outer target which have ionized after being emitted towards the plasma along any flux tube (each level corresponds to an increase of 10%).

While the correlation of plasma profiles between midplane and ionization front is easily explained by pressure conservation, the exact correlation between ionization front and divertor target cannot be established with accuracy, because of the strong momentum losses occurring between the two locations. However, in view of the presented results, an at least qualitative connection between midplane plasma profiles and target recycling profiles appears plausible. This is, indeed, consistent with most of the neutrals contributing to the far SOL ionization source upstream being originated from target recycling (see figure 9). Additionally, this is also consistent with the experimental observation, made not only at JET [14] but also at AUG [34] of the D_α emission in the outer divertor region moving further from the separatrix following the onset of the shoulder formation.

4.5. Proposed mechanism for shoulder formation

Summarizing, the results presented in this section are consistent with different findings reported in the literature. In agreement with the numerical EMC3-EIRENE results presented by Carralero *et al* [12], SOLPS-ITER as well indicates the existence of an enhanced ionization in the far SOL when a density shoulder is present. Moreover, consistently with

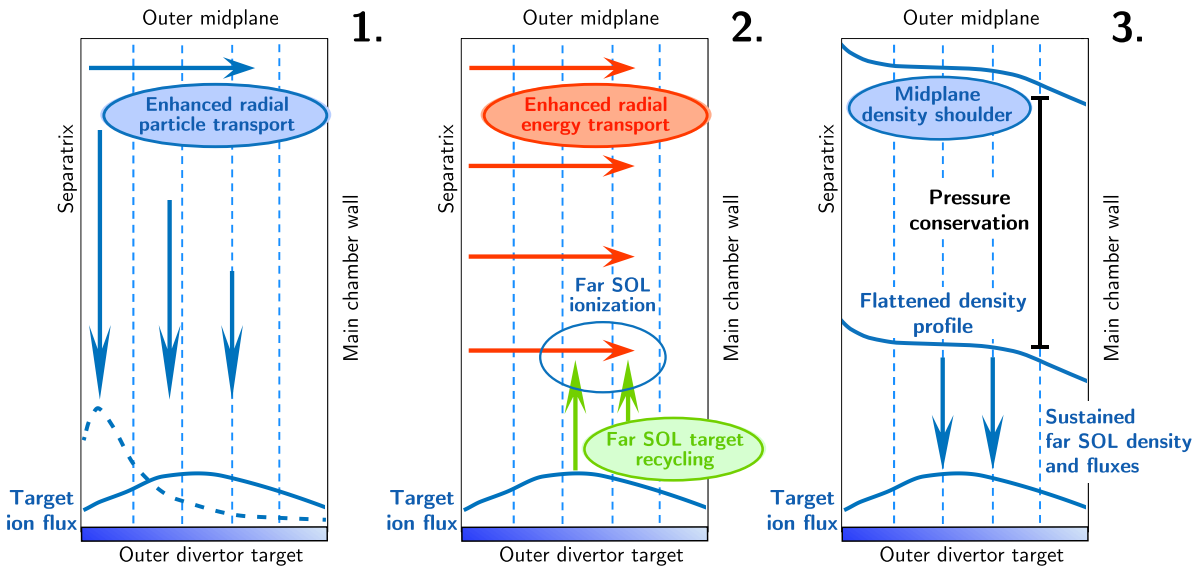

Figure 11. Proposed mechanism for the shoulder formation according to the presented results. 1. The enhanced radial particle transport causes ions to strike the target further away from the separatrix. 2. The resulting recycling profile leads to a larger neutral population in the far SOL flux tubes. The larger amount of energy transported towards the far SOL triggers the ionization of such neutrals. 3. The enhanced far SOL ionization accounts for the 'additional' plasma particles to flatten the density profile at the poloidal location where the target-recycled neutrals are ionized. Through pressure conservation, the midplane profile results flattened as well. At the same time the high density in the far SOL sustains elevated ion fluxes to the far SOL target, closing the loop.

the experimental observations made at JET by Wynn *et al* [14], SOLPS-ITER indicates the presence of an interplay between shoulder formation and divertor neutral recycling processes.

The performed analysis of various aspects of the numerical plasma solutions suggests the following mechanism for the shoulder formation at the outer SOL midplane, pictured in figure 11:

(1) The enhancement of perpendicular transport in the SOL causes, in first instance, a reshaping of the ion flux profile onto the target towards flux tubes further away from the separatrix (see left plot in figure 7).
(2) The modified recycling profile may imply the presence of a larger neutral population in the far SOL flux tubes. The larger amount of energy transported towards the far SOL (see right plot in figure 5) is able to supply the energy cost needed for ionizing more neutrals, triggering an enhanced far SOL ionization (see figures 6 and 9).
(3) This implies an elevated plasma density in the far SOL upstream. At the same time a large ion flux striking the target far from the separatrix is sustained, finally closing a 'loop' which had been first initiated by the enhanced perpendicular transport.

5. Perpendicular transport and divertor detachment

The second matter of investigation accounted for the processes involved in the detachment of the outer divertor target in conditions of enhanced perpendicular SOL transport. Such experimentally revealed feature was correctly reproduced by the simulations as well (figure 7).

5.1. Analytical models and previous studies

In the literature it is widely accepted that the mutually complementary effects of the increase of radiation power losses and volumetric recombination are the processes causing a drop in the parallel ion flow before it reaches the targets in detached conditions [35]. According to a simple 2PM analysis of the SOL plasma the access of a detached regime is also intimately related to an increase of the momentum losses in the plasma from upstream to target [29]. The ion flux striking the target can be shown, indeed, to be reduced by a factor which scales with the square of the total pressure drop between upstream and target. Such a correlation between increase of momentum losses and detachment onset has been confirmed both experimentally and numerically by Paradela Pérez *et al* [36].

However, it is still debated if a causality relationship exists between momentum losses and reduction of the ion flux. According to Krasheninnikov and Kukushkin [15], momentum losses would be a mere complementary feature arising from processes (e.g. CX collisions) which are effective at low temperatures, i.e. the same temperatures which facilitate recombination processes. A more advanced analytical model recently developed by Stangeby [16, 17] suggests that the increase of momentum losses along the SOL is, instead, critical in directly causing the ion flux rollover.

On the other hand, the correlation between collisionality regimes, intensity of perpendicular transport and detachment onset has been already investigated numerically by Wiesen *et al* [37]. The ion flux rollover during a fueling ramp was seen to be facilitated by the application of a model in which the intensity of perpendicular transport scales with the collisionality. This already showed a direct impact which an increased

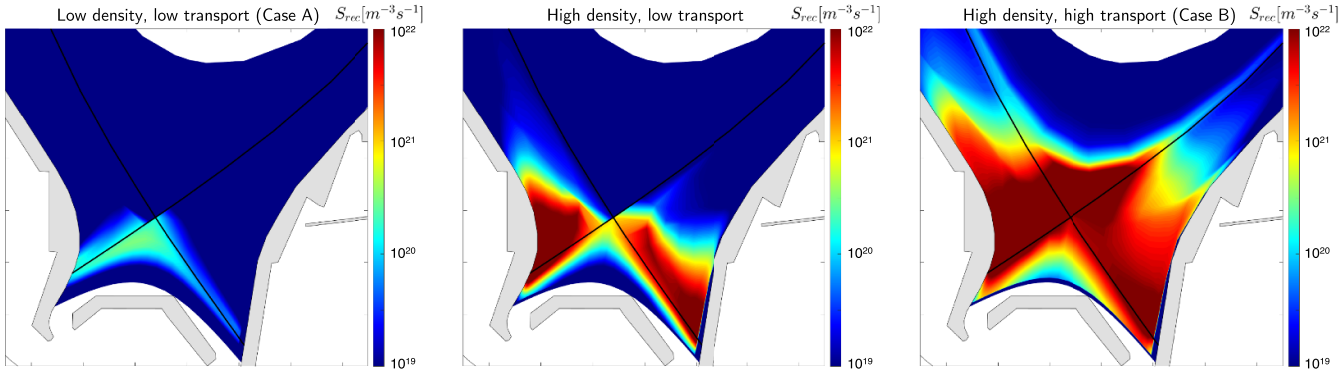

Figure 12. 2D distributions of the recombination rate in the divertor region for all cases.

transport has in causing the detachment. However, no thorough investigation was performed about the physical mechanisms relating these two aspects.

Analyzing the numerical plasma solutions we tried to identify and quantify the physical mechanisms which lead to the detachment in conditions of enhanced transport, and, at the same time, to establish role and relevance of momentum losses in achieving it.

5.2. Role of volumetric recombination

According to figure 7, increasing the density was sufficient to achieve the 'power detachment', i.e. the complete flattening of the heat flux density profile at the outer target. This is consistent with a power loss factor for the SOL (equation (4)) having reached already a large and almost saturated value in the modelled intermediate high density, low transport case. On the other hand, the achievement of the 'plasma detachment', i.e. a relevant flattening of the ion flux profile, was possible only after the increase of transport. In the intermediate case, the ion flux onto the target was still large and peaked close to the separatrix.

For the ion flux to drop in a relevant way from low transport to high transport cases, in spite of these having the same density regime (i.e. same $n_{e,sep}$), the intensity of recombination must have increased. Plotting the 2D distributions of the recombination rate in the divertor (figure 12) reveals, indeed, that recombination is much more relevant after the increase of transport. This is especially true for the flux tubes close to the separatrix, i.e. precisely where the ion flux onto the target drops.

5.3. Role of radial momentum transport

We investigated then which is the physical mechanism, mainly effective only after the increase of transport, which might make the recombination rise. Looking at figure 8 reminds that the relative intensity of momentum losses is similar between high density, low transport case and high density, high transport case. However, the last one features a radial shift of the total pressure peak at the outer target, as a consequence of pressure being completely removed from the near-separatrix flux tubes. This is consistent with the ion flux being flattened precisely on the near-strikepoint portion of the target (left plot in figure 7).

We checked what makes the pressure completely disappear from the near-separatrix flux tubes only after the transport enhancement. For doing this we decomposed the total poloidally-integrated momentum source term considered in the section 3.5, i.e. the yellow lines in figure 8, in all its individual components as computed by SOLPS-ITER. The results for all cases are shown in figure 13. See again appendix B for more details.

As one could expect, the bulk increase of momentum losses when moving from low to high density is driven by a stronger presence of plasma-neutral interactions (e.g. CX collisions). This mainly originates from the cooling down of the divertor after the density increase, which lowers the temperature sufficiently to promote these processes, while simultaneously sustaining high recycling levels.

However, the complete drop off of pressure onto the near-strikepoint portion of the target, occurring only after the transport enhancement, can be attributed to another loss component, whose intensity is represented by the yellow lines in figure 13. This is caused by the mechanism of radial momentum transport. This consists in momentum being gained in or removed by each flux tube directly due to perpendicular particle transport. Increased flows of particles radially directed towards the far SOL, indeed, can remove from the near SOL the momentum which is carried by such particles.

This term is always negligible in the two low transport cases with respect to the total loss. In the high transport case, instead, its relative contribution in the total loss is not negligible: it removes up to 30% of the total momentum from the flux tubes close to the separatrix, resulting in an even stronger momentum removal than the one solely caused by plasma-neutral interactions. Albeit remaining secondary in relative magnitude with respect to the loss due to plasma-neutral interactions, this mechanism is effective enough to allow for some redistribution of momentum from the near SOL to the far SOL. This explains the radial shift to the far SOL of the peak of the pressure profile onto the target.

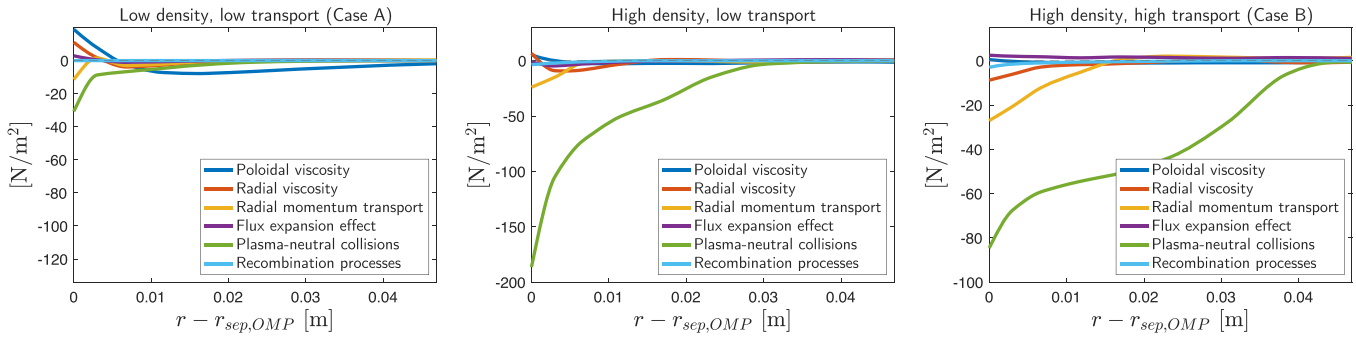

Figure 13. Decomposition of the total poloidally-integrated momentum source between upstream and downstream for all cases, according to the parallel momentum balance analysis performed in the section 3.5. The sum of all these types of losses corresponds to the yellow lines in the plots in figure 8. Radial coordinates are remapped to the one at the outer midplane.

5.4. Proposed mechanism for divertor detachment

After the power balance performed in the section 3.4, we found that the transport enhancement alone does not contribute much in removing more power from the plasma. This analysis is consistent with the heat flux profile at the outer target being already flattened after the mere increase of density, i.e. even without increasing the transport (right plot in figure 7). The increase of power losses, arising mainly after the density increase, is not sufficient alone in driving the processes (such as recombination) which make the ion flux drop before striking the targets. Indeed, they are not able to detach the plasma from the target in the high density, low transport scenario.

According to the results presented in this section, the transport enhancement does contribute instead in a relevant way in removing more pressure at least in the near-separatrix flux tubes, redistributing momentum towards the far SOL. We believe that this feature likely plays a key role in the achievement of a detached regime, which was experimentally observed and numerically reproduced. This is consistent with a drop in the ion flux onto the target occurring only in the high density, high transport scenario (left plot in figure 7).

We assume that what physically occurs is the following. The increase of power dissipation by radiation, following the increase of density, cools down the plasma near the targets. The complete removal of pressure in the near-separatrix flux tubes, occuring after the increase of transport, contributes to slow down the plasma flow in these flux tubes. Such situation finally increases the residence time of electrons and ions in a cold divertor. This ultimately promotes a stronger presence of recombination processes (see figure 12), which makes a large quantity of plasma particles 'disappear' before reaching the targets, at least close to the strikepoint.

The combination of both strong momentum and power losses is then necessary to detach the divertor plasma, at least in the performed simulations. Without the further pressure drop occurring after transport enhancement in the near-separatrix flux tubes, driven by momentum redistribution, recombination would not have been strong enough to drop the ion flux onto the near-strikepoint portion of the target.

Overall, these results confirm the presence of a direct link between perpendicular particle transport in the SOL and the access to a detached regime for the divertor, as already suggested by Wiesen *et al* [37]. Additionally, they support the idea, motivated by the analytical calculations performed by Stangeby [16, 17], of momentum losses being a necessary ingredient for the detachment to take place, in addition to the power losses.

6. Summary and outlook

The thorough analysis performed in this work allowed us to characterize the impact of an enhanced perpendicular transport regime, experimentally observed at the AUG tokamak, on the global plasma behaviour and the exhaust processes. The performed SOLPS-ITER simulations provided quite realistic results, despite the imposition of some simplifications.

Imposing extremely high values of an effective particle diffusivity (of the order of tens $\mathrm{m^2\ s^{-1}}$) was required for matching the experimental measurements. Such coefficient provides a steady-state average of the effects of intermittent filament-driven advective transport. This is justified by existing theoretical models, and allowed us to correctly reproduce the main experimental findings, i.e. the shoulder formation and a partial detachment.

One direct consequence of the transport enhancement is a significant increase of radial energy transport at the midplane. This is mainly driven by a convective component, as more particles carry heat with them. This leads to a large fraction of the SOL input power still present at the midplane even several cm away from the separatrix, prevailing over the parallel losses. We assume that this is the main mechanism relating enhanced transport and shoulder formation. Namely, this contributes to bring a sufficient amount of energy in the far SOL for sustaining an increased ionization rate of neutrals mainly originating from target recycling. This provides a source of plasma particles which is sufficient to balance the parallel losses and produce a flattening of the radial density profile. The results also suggest that the recycling at the main wall surface, which is however increased, might not be a relevant mechanism in providing the neutrals which are ionized to form the shoulder.

A drastic drop of both ion and heat fluxes striking the outer target in the near-strikepoint portion is also observed following the increase of transport. A quantitative analysis of momentum and power dissipation in the SOL plasma allowed us to observe that both types of losses are increased in this condition. The relative intensity of power-removing processes is mainly driven by the mere increase of density. Momentum losses, instead, are even more increased following the transport enhancement, at least in the near-separatrix flux tubes. This is due to a momentum redistribution from the near SOL to the far SOL directly caused by the increase of transport. We assume that this might contribute in a significant way to access a detached regime, dropping the ion flux on the near-strikepoint portion of the target.

Although the results are in a satisfyingly good agreement with the experiments, further modelling efforts might be devoted to improve these. Drifts and currents in the transport equations solved by B2.5 may be fully activated. This could allow to investigate further features, e.g. how asymmetries between inner and outer divertor respond to the transport enhancement. Furthermore, a more realistic prediction about the impact of main wall recycling on the density shoulder formation might be possible in the near future, as soon as SOLPS-ITER will allow using a computational grid that extends up to the physical walls.

The research concerning perpendicular transport in the SOL plasma is turning out to be of critical importance for predicting the operation of future fusion reactors. The transition in perpendicular transport has been experimentally related to the onset of a density shoulder at the midplane and to the access of a detached regime for the divertor under a wide range of scenarios in devices featuring ITER-like geometry and PFCs. Since future tokamaks will certainly operate with highly collisional divertors, an enhanced perpendicular transport regime could likely be present as well. We suggest then to validate this type of numerical investigation against experiments in more devices and in more different plasma scenarios (e.g. high power H-modes or alternative divertor configurations).

Data availability statement

The data that support the findings of this study are available upon reasonable request from the authors.

Acknowledgments

The authors are grateful to R Fischer for the support about the working principles of the IDA diagnostics at AUG, to F Reimold and B Tal for the inspiring discussions about the interpretation of the numerical plasma solutions, and to D Moulton for providing the MATLAB routines used for the parallel momentum balance analysis. This work has been carried out within the framework of the EUROfusion Consortium and has received funding from the Euratom research and training program 2014–2018 and 2019–2020 under Grant Agreement No. 633053. The views and opinions expressed herein do not necessarily reflect those of the European Commission.

Appendix A. Description of the employed iterative fitting algorithm

In this appendix we describe the algorithmic optimization procedure for the main input parameters to be imposed in the SOLPS simulations, employed to achieve the final plasma solutions. The entire procedure, which was performed both for case A and for case B, is graphically summarized in figure 14.

(1) *Collecting the experimental radial profiles for density and temperature for the considered scenarios*.
We collected the experimental radial n_e and T_e profiles measured at the outer midplane in the AUG discharge #33341 at the considered times, as a function of the major radius coordinate R. For the electron density profiles, as already mentioned, we used the results of the IDA performed at AUG [23]. For the electron temperature profiles, instead, we used the edge Thomson Scattering (TS) data [38].

(2) *Making assumptions for the estimation of the position of the separatrix*.
For properly modelling the midplane conditions, in SOLPS-ITER a 'target value' for $n_{e,sep}$ based on the corresponding experimental estimation could be imposed. This will be achieved during the run through a feedback mechanism regulating the particle source into the computational domain.

For a correct experimental estimation of $n_{e,sep}$, it is necessary to estimate the major radius position R_{sep} of the separatrix as well (which we considered unknown *a priori*). The employed strategy for doing this was to couple the experimental knowledge of the density and temperature profiles at the midplane with the results of the simulations in a self-consistent way. The expected goal was that the experimental estimation of $T_{e,sep}$, corresponding to the assumed separatrix positions, results as close as possible to the modelled $T_{e,sep}$ value.

First, we assumed some different possible values for $T_{e,sep}$ (in the realistic range 25–70 eV). Then, according to an exponential fit of the TS data, we selected the values of R_{sep} which correspond to the various possible $T_{e,sep}$ values. Finally, assuming the TS and IDA data being referred to the same radial coordinate (i.e. having no radial shift relative to each other), we found the values of $n_{e,sep}$ which correspond to the various possible values of R_{sep} (i.e. in turn, to the possible values of $T_{e,sep}$).

Ultimately we had a set of possible assumptions, each one corresponding to a triplet $(T_{e,sep}, R_{sep}, n_{e,sep})$.

(3) *Performing a SOLPS scan over all made assumptions, optimizing the anomalous particle diffusivity*.
For both cases we carried out the corresponding set of feedback-controlled SOLPS runs, each one using the possible different targeted $n_{e,sep}$ values as physical input, i.e. corresponding to a single triplet $(T_{e,sep}, R_{sep}, n_{e,sep})$.

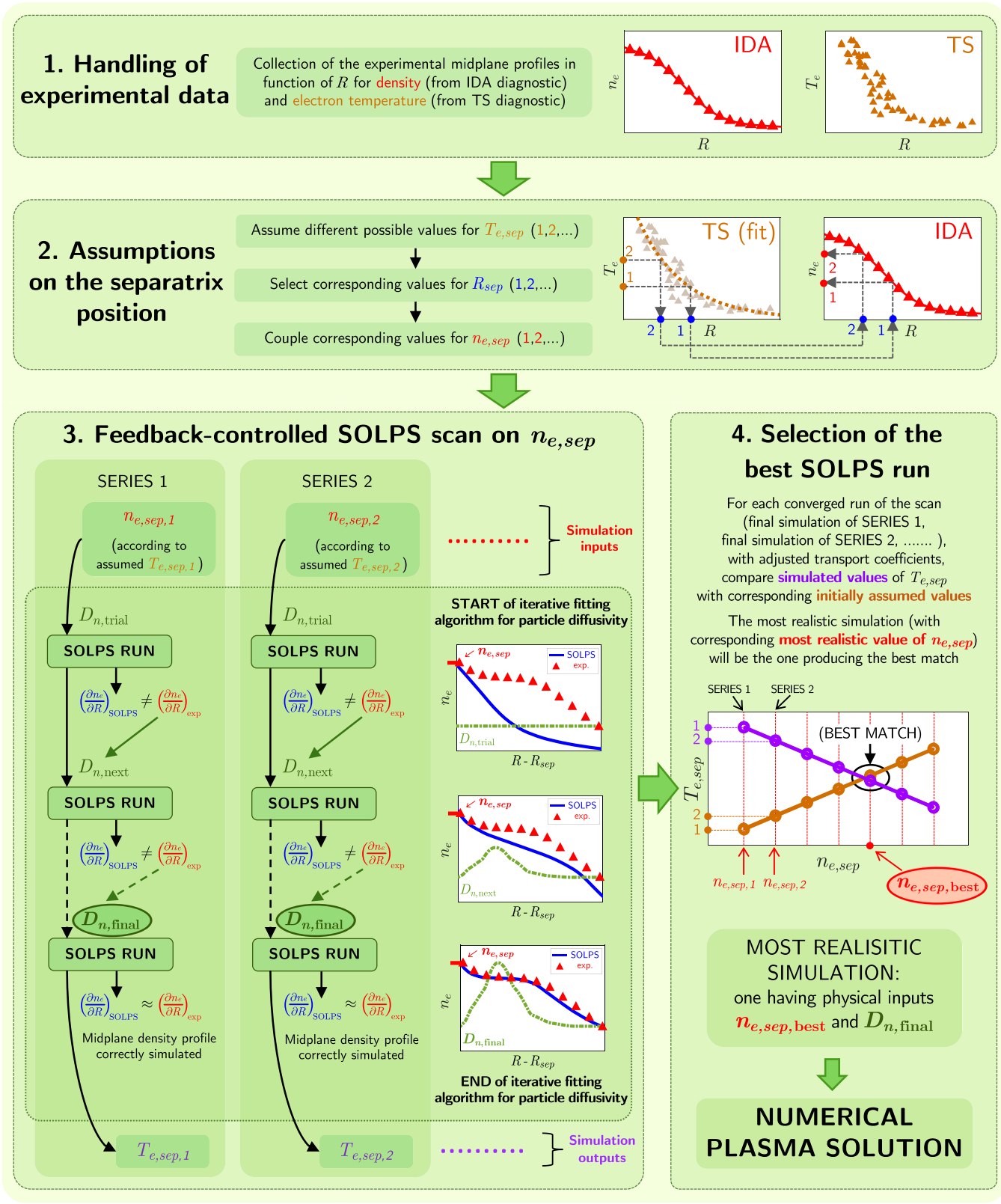

Figure 14. Flow diagram of the modelling activity which was carried out, in order to face with the uncertainties in the imposition of the density regime (i.e. a value of $n_{e,sep}$ at the outer midplane) and the assumption for the perpendicular transport (i.e. a radial profile of D_n). The simulations whose results were presented in the text for both cases A and B are the ones using, as physical inputs, the $n_{e,sep}$ values and the D_n profiles resulting from this procedure.

In this step, for all simulations we employed an iterative algorithm, similar to what already done in [39], in order to 'adjust' the radial profiles of the effective particle diffusivity D_n. This was the key step of the entire modelling activity, as it made possible to match the experimental radial density profiles with the simulation results. This relies on the fact that, if $n_{e,sep}$ is kept as a fixed targeted parameter in the simulations, then the modelled density profile $n_e(R - R_{sep})$ in the SOL can be fully described by its radial gradient $\frac{\partial n_e(R-R_{sep})}{\partial R}$ in each point.

The modelled radial density gradient was controlled by adjusting D_n in the following way:

- We started with a 'trial' uniform transport profile $D_{n,\mathrm{trial}}$. Correspondingly, we performed SOLPS runs for each possible $n_{e,sep}$ assumption using such trial transport profile (i.e. imposing $n_{e,sep,1}$, $n_{e,sep,2}$, etc as targeted values). After convergence of the simulations, the modelled radial density gradient $\left(\frac{\partial n_e}{\partial R}\right)_{\mathrm{SOLPS}}$ could be different from the experimental one $\left(\frac{\partial n_e}{\partial R}\right)_{\mathrm{exp}}$.
- According the SOLPS equations, the modelled radial particle flux density is computed as

$$\Gamma_{\perp,\ \mathrm{SOLPS}} = -D_{n,\mathrm{trial}} \left(\frac{\partial n_e}{\partial R}\right)_{\mathrm{SOLPS}}. \tag{8}$$

  In this way a possible 'next-step' value for the particle diffusivity at each radial location of the SOL, which should produce a radial density gradient more similar to the experimental one, can be calculated as

$$D_{n,\mathrm{next}} = -\frac{\Gamma_{\perp,\ \mathrm{SOLPS}}}{(\partial n_e/\partial R)_{\mathrm{exp}}}. \tag{9}$$

- For each $n_{e,sep}$ assumption, we used this new transport profile as input for new runs, yielding a new modelled radial density gradient. If this was still different from the experimental one, the procedure was repeated once more.
- After very few steps we achieved a 'final' transport profile $D_{n,\mathrm{final}}$. The corresponding simulations finally gave a modelled radial density gradient similar to the experimental one at each radial location.

At the conclusion of the iterative fitting algorithm, a set of simulations reached convergence, each one run with different targeted values of the midplane separatrix density and corresponding to a different assumption for the position of the separatrix (i.e. to a different assumed triplet ($T_{e,sep}$, R_{sep}, $n_{e,sep}$)). Ultimately, each simulation produced a different modelled value of $T_{e,sep}$.

(4) *Selecting the most realistic simulation*.
The criterion for selecting the best assumption for the position of the separatrix (i.e. the most realistic assumed triplet ($T_{e,sep}$, R_{sep}, $n_{e,sep}$)) was to choose that one providing the best match between the initially assumed value of $T_{e,sep}$ and corresponding simulated value. An unequivocal choice for this was possible. Indeed, triplets with assumed higher values of $T_{e,sep}$ contains higher values of $n_{e,sep}$ as well (since the assumed separatrix position would be located more radially inward). Vice versa, imposing increasing values of $n_{e,sep}$ as input for the simulations provided a decrease in the modelled values of $T_{e,sep}$. So, an 'optimum point' could be identified, i.e. the simulation whose assumed and simulated $T_{e,sep}$ values are closest, and whose separatrix density $n_{e,sep,\mathrm{best}}$ is then the most realistic one.

Ultimately, the simulation using such density $n_{e,sep,\mathrm{best}}$ as targeted input and featuring the transport profile $D_{n,\mathrm{final}}$ was selected, and the corresponding numerical plasma solution studied.

Table 2. Data about the performed simulations in the framework of the employed fitting procedure. For both cases A and B the initial assumptions for $T_{e,sep}$, the resulting coupled experimental R_{sep} and $n_{e,sep}$ values and the simulated $T_{e,sep}$ values are shown. The simulations which produced the best agreement between assumed and simulated $T_{e,sep}$ (i.e. the ones from which we extracted the final plasma solutions) are highlighted in bold.

Case A			
Assumed $T_{e,sep}$ (eV)	*Corresp.* R_{sep} (m)	*Resulting experim.* $n_{e,sep}$ (10^{19} m^{-3})	*Simulated* $T_{e,sep}$ (eV)
45	2.140	0.64 (±0.05)	68.8
50	2.139	0.68 (±0.05)	67.2
55	2.137	0.72 (±0.05)	65.7
60	2.136	0.75 (±0.06)	64.6
65	**2.135**	**0.78 (±0.06)**	**63.6**
70	2.134	0.81 (±0.06)	62.6
Case B			
Assumed $T_{e,sep}$ (eV)	*Corresp.* R_{sep} (m)	*Resulting experim.* $n_{e,sep}$ (10^{19} m^{-3})	*Simulated* $T_{e,sep}$ (eV)
25	2.142	1.41 (±0.18)	31.5
30	**2.139**	**1.52 (±0.18)**	**29.7**
35	2.136	1.63 (±0.19)	25.5
40	2.134	1.78 (±0.20)	22.5
45	2.132	1.92 (±0.20)	‡
50	2.131	2.04 (±0.21)	‡

‡ Simulations crashed due to non-linear behaviour caused by elevated density and low divertor temperature.

Table 2 shows assumed triplets ($T_{e,sep}$, R_{sep}, $n_{e,sep}$) and subsequent simulated $T_{e,sep}$ values for both cases:

- For case A the best assumption selected for $T_{e,sep}$ was 65 eV, corresponding to a separatrix density of 0.78(±0.06) $\times 10^{19}$ m^{-3}.
- For case B the best assumption selected for $T_{e,sep}$ was 30 eV, corresponding to a separatrix density of 1.52(±0.18) $\times 10^{19}$ m^{-3}.

The simulations imposing the $n_{e,sep}$ values of 0.78 and 1.52 ($\times 10^{19}$ m^{-3}) are the ones whose results were described in the rest of the text. The uncertainty in the numerical results, which

was included by adding confidence bands in various plots, was estimated using the experimental uncertainty of the IDA data, i.e. running simulations for the upper and lower bounds of $n_{e,sep}$ as well.

Appendix B. Derivation of the two-point relation for the parallel momentum balance equation

In this appendix we briefly summarize the derivation of the integral balance equation for parallel momentum in the SOL plasma between two different poloidal locations, thoroughly explained in [30], whose results for the modelled case were shown in figures 8 and 13.

Because of the mapping of the physical curvilinear poloidal and radial coordinates in an orthogonal system performed by B2.5 (i.e. $(\theta, r) \rightarrow (x, y)$), the use of metric coefficients h_x, h_y is necessary. The quantity $\sqrt{g}$ represents the jacobian of the coordinate transformation between the two systems.

For a purely hydrogenic plasma (i.e. $Z_{\text{eff}} = 1$, $n_i = n_e$) the steady-state form of the parallel momentum balance equation solved by B2.5 is [20]:

$$\frac{1}{\sqrt{g}}\frac{\partial}{\partial x}\left(\frac{\sqrt{g}}{h_x}\pi_x\right) + \frac{1}{\sqrt{g}}\frac{\partial}{\partial y}\left(\frac{\sqrt{g}}{h_y}\pi_y\right) + \frac{B_\theta}{B}\frac{1}{h_x}\frac{\partial p}{\partial x} = S_{\text{mom,vol}}. \tag{10}$$

Here π_x, π_y are the poloidal and radial momentum flux density, respectively, given by

$$\pi_x = m_i \Gamma_x v_\parallel - \eta_x \frac{1}{h_x}\frac{\partial v_\parallel}{\partial x} \tag{11}$$

$$\pi_y = m_i \Gamma_y v_\parallel - \eta_y \frac{1}{h_y}\frac{\partial v_\parallel}{\partial y}. \tag{12}$$

Both have a component associated with the poloidal/radial particle transport (Γ_x, Γ_y being the poloidal/radial particle flux densities, and $v_\parallel$ the parallel flow velocity) and a component associated to viscous effects (η_x, η_y being the poloidal/radial classical ion viscosity components). $p = n_e(T_e + T_i)$ is the static pressure. $S_{\text{mom,vol}}$ is the volumetric momentum source density which, in the considered cases, only includes the source due to plasma-neutral interactions (e.g. CX collisions) and to recombination computed by EIRENE.

The quantity for which an integral balance equation is desired is $\frac{B_\theta}{B}(p + m_i n_e v_\parallel^2)$. This is the poloidal projection of the total pressure force acting in parallel direction along a given flux tube. In order to do this, the static pressure present on the L.H.S. of the equation (10) is moved inside the divergence term $\frac{1}{\sqrt{g}}\frac{\partial}{\partial x}\left[\frac{\sqrt{g}}{h_x}(\quad)\right]$. This allows, after some calculations, to isolate the term describing a poloidal balance of the total pressure as

$$\frac{1}{\sqrt{g}}\frac{\partial}{\partial x}\left[\frac{\sqrt{g}}{h_x}\frac{B_\theta}{B}(p + m_i n_e v_\parallel^2)\right] = S_{\text{mom,tot}}. \tag{13}$$

All the terms of the equation (13) can be finally integrated between two different poloidal upstream and downstream locations, as $\int_{up}^{down}(\quad)\sqrt{g}\,dxdy$, or $\int_{x_{up}}^{x_{down}}(\quad)A(x)h_x dx$, being

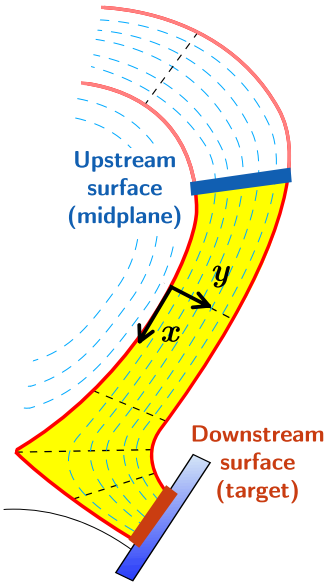

Figure 15. Sketch of the volume of the SOL plasma in which the total poloidally-integrated momentum losses, plotted in figures 8 and 13, are computed. Highlighted are also the upstream and downstream surfaces to which the pressure profiles plotted in the figure 8 are referred.

$A(x)$ the poloidal-directed elementary area on a radial surface. This finally yields the two-point relation for the parallel momentum balance:

$$\left[\frac{B_\theta}{B}A_x(p + m_i n_e v_\parallel^2)\right]_{down} - \left[\frac{B_\theta}{B}A_x(p + m_i n_e v_\parallel^2)\right]_{up} = \int_{x_{up}}^{x_{down}} S_{\text{mom,tot}} h_x A_x\, dx. \tag{14}$$

Equation (14) is the relation which is plotted for all modelled cases for each flux tube of the radial domain of the SOL in figure 8. The upstream surface was at the outer midplane, while the downstream surface was at the outer target. Therefore, the volume over which the poloidally-integrated momentum losses were computed is the one sketched in figure 15. In order to have a consistent balance of the total pressure force (in N m^{-2}) between such two different poloidal locations, each term of the equation (14) is divided by the value of $\frac{B_\theta}{B}A_x$ taken at the target when plotted in figure 8.

Furthermore, the total source term $S_{\text{mom,tot}}$ can be splitted in its different components. According to the calculations yielding the equation (13), this can be written as

$$\begin{aligned} S_{\text{mom,tot}} = {} & \frac{1}{\sqrt{g}}\frac{\partial}{\partial x}\left(\frac{\sqrt{g}}{h_x^2}\eta_x\frac{\partial v_\parallel}{\partial x}\right) + \frac{1}{\sqrt{g}}\frac{\partial}{\partial y}\left(\frac{\sqrt{g}}{h_y^2}\eta_y\frac{\partial v_\parallel}{\partial y}\right) \\ & - \frac{1}{\sqrt{g}}\frac{\partial}{\partial y}\left(\frac{\sqrt{g}}{h_x}m_i\Gamma_y v_\parallel\right) \\ & + p\frac{1}{\sqrt{g}}\frac{\partial}{\partial x}\left(\frac{\sqrt{g}}{h_x}\frac{B_\theta}{B}\right) + S_{\text{mom,vol.}} \end{aligned} \tag{15}$$

Following the order in which these appear in the equation (15), the various momentum loss mechanisms are: viscous

effects due to the poloidal gradient of the flow velocity, viscous effects due to the radial gradient of the flow velocity, direct radial momentum transport, geometrical effect due to flux expansion between different portions of a flux tube, and volumetric processes computed by EIRENE (i.e. plasma-neutral interactions and recombination). The resulting decomposition of the R.H.S. of the equation (14) is that shown in figure 13.

ORCID iDs

A Zito https://orcid.org/0000-0002-6743-6568
D Carralero https://orcid.org/0000-0002-7824-3307
P Manz https://orcid.org/0000-0002-5724-0174
M Passoni https://orcid.org/0000-0002-7844-3691

References

[1] Zohm H *et al* 2013 *Nucl. Fusion* **53** 073019
[2] Wischmeier M 2015 *J. Nucl. Mater.* **463** 22–9
[3] Wischmeier M *et al* 2018 *27th IAEA Fusion Conf., (Gandhinagar)*
[4] Zweben S J and Gould R W 1985 *Nucl. Fusion* **25** 171
[5] Boedo J A *et al* 2001 *Phys. Plasmas* **8** 4826
[6] D'Ippolito D A *et al* 2011 *Phys. Plasmas* **18** 060501
[7] Krasheninnikov S I 2001 *Phys. Lett.* A **283** 368–70
[8] Krasheninnikov S I *et al* 2008 *J. Plasma Phys.* **74** 679
[9] Myra J R *et al* 2006 *Phys. Plasmas* **13** 112502
[10] Carralero D *et al* 2014 *Nucl. Fusion* **54** 123005
[11] Carralero D *et al* 2015 *Phys. Rev. Lett.* **115** 215002
[12] Carralero D *et al* 2017 *Nucl. Fusion* **57** 056044
[13] Carralero D *et al* 2018 *Nucl. Fusion* **58** 096015
[14] Wynn A *et al* 2018 *Nucl. Fusion* **58** 056001
[15] Krasheninnikov S I and Kukushkin A S 2017 *J. Plasma Phys.* **83** 155830501
[16] Stangeby P C 2020 *Plasma Phys. Control. Fusion* **62** 025012
[17] Stangeby P C 2020 *Plasma Phys. Control. Fusion* **62** 025013
[18] Wiesen S *et al* 2015 *J. Nucl. Mater.* **463** 480–4
[19] Bonnin X *et al* 2016 *Plasma Fusion Res.* **11** 1403102
[20] Schneider R *et al* 2006 *Contrib. Plasma Phys.* **46** 3–191
[21] Braams B J 1986 Computational studies in tokamak equilibrium and transport PhD Thesis Rijksuniversiteit Utrecht
[22] Reiter D *et al* 2005 *Fusion Sci. Technol.* **47** 172–86
[23] Fischer R *et al* 2010 *Fusion Sci. Technol.* **58** 675–84
[24] Fischer R *et al* 2003 *Plasma Phys. Control. Fusion* **45** 1095
[25] Aho-Mantila L *et al* 2017 *Plasma Phys. Control. Fusion* **59** 035003
[26] Manz P *et al* 2020 *Phys. Plasmas* **27** 022506
[27] Carralero D *et al* 2018 *23th Int. Conf. on PSI in Controlled Fusion Devices (Princeton)*
[28] Kallenbach A *et al* 2015 *Nucl. Fusion* **55** 053026
[29] Stangeby P C 2000 *The Plasma Boundary of Magnetic Fusion Devices* (Boca Raton, FL: CRC Press)
[30] Kotov V and Reiter D 2009 *Plasma Phys. Control. Fusion* **51** 115002
[31] Lipschultz B *et al* 2005 *Plasma Phys. Control. Fusion* **47** 1559–78
[32] LaBombard B *et al* 2000 *Nucl. Fusion* **40** 2041
[33] Lunt T *et al* 2015 *J. Nucl. Mater.* **463** 744–7
[34] Agostini M *et al* 2019 *Plasma Phys. Control. Fusion* **61** 115001
[35] Krasheninnikov S I *et al* 2016 *Phys. Plasmas* **23** 055602
[36] Paradela Pérez I *et al* 2017 *Nucl. Mater. Energy* **12** 181–6
[37] Wiesen S *et al* 2011 *J. Nucl. Mater.* **415** 535–9
[38] Kurzan B *et al* 2011 *Rev. Sci. Instrum.* **82** 103501
[39] Canik J M *et al* 2011 *J. Nucl. Mater.* **415** 409–12